npj | 2D materials and applications

Article

Published in partnership with FCT NOVA with the support of E-MRS

https://doi.org/10.1038/s41699-024-00464-x

# Enhancing dielectric passivation on monolayer $WS_2$ via a sacrificial graphene oxide seeding layer



P.-J. Wyndaele[1,2] ✉, J.-F. de Marneffe[2], S. Sergeant[2], C. J. L. de la Rosa[2], S. Brems[2], A. M. Caro[3] & S. De Gendt[1,2]

The full utilization of two-dimensional transition metal dichalcogenides (2D TMDCs) faces several challenges, among which is realizing uniform material deposition on the 2D surface. Typical strategies to enable material growth lead to a poor interface quality, degrading the 2D TMDC's properties. In this work, a sacrificial, graphene oxide-based seeding layer is used (1) as passivation layer, protecting the underlying 2D TMDC and (2) as nucleation layer, enabling uniform material growth. Graphene is transferred on monolayer $WS_2$, establishing a high-quality van der Waals interface. After transfer, the polymeric residues on graphene are cleaned via a combination of wet- and dry treatments and functionalized via dry UV/$O_3$ oxidation. The rate of graphene oxidation is shown to be substrate dependent, which is explained by UV light-induced ultrafast charge transfer between the graphene and $WS_2$ monolayer. The carbon-oxygen functionalities serve as nucleation sites in a subsequent $HfO_2$ ALD process, achieving more uniform dielectric growth and faster layer closure compared to direct deposition. The graphene-based nucleation- / passivation approach offers adaptability, allowing for tailored surface chemistry to enable any alternative material growth, while maintaining a prefect van der Waals interface.

Two-dimensional transition metal dichalcogenides (2D TMDC's), often depicted as $MX_2$ (M = W, Mo, … & X = S, Se, …), have attracted substantial interest due to a wide variety of applications including catalysis, energy storage and microelectronic devices[1]. For microelectronic applications, 2D TMDC's are promising alternatives or supplements for today's silicon-based technology, owing to their inherent ultra-thin structure enabling superior electrostatic gate control and carrier confinement compared to 3D bulk semiconductors[2,3]. In addition, 2D TMDC's have a high carrier mobility[4], sizeable band-gaps[5] and the potential for defect-free interfaces resulting from their smooth, self-passivated surfaces free of dangling bonds[6].

However, the lack of dangling bonds does not allow for uniform material growth when done directly on the $MX_2$ surface, which is critical for many microelectronic- and other applications. Nucleates only grow at defect sites or less stable areas such as grain boundaries, which have a low density in highly crystalline films. This results in island-like growth and poor quality of the deposited material[7].

Enhancing material growth requires increasing the number of nucleation sites i.e., functionalizing the $MX_2$ surface either via a covalent- or non-covalent approach. In the covalent approach, molecules are grafted on the $MX_2$ surface leading to chemical functionalization for which the density of grafted molecules is often difficult to control and not stable at elevated temperatures[8,9]. For example, Azcatl et al. greatly enhanced dielectric deposition on multilayer $MoS_2$, $MoSe_2$, and $WSe_2$ surfaces via UV/$O_3$ exposure, generating an oxygen-terminated surface that was 'self-cleaned' after atomic layer deposition (ALD) at high temperatures[10,11]. Follow-up studies by Zhao et al. revealed various electrically active traps at the dielectric/$MX_2$ interface, which could be ameliorated by high temperature anneals[12,13]. The electrically active traps originated from unintentional doping of the upper layer during UV/$O_3$ functionalization, protecting the underlying layers. Multilayer $MX_2$ films are inherently less susceptible to surface effects compared to monolayer systems, whose properties are drastically changed upon chemical bond formation[8]. In the non-covalent approach, physisorbed molecules interact via van der Waals (vdW) forces or electrostatic interactions. Since the physisorbed molecules are only weakly bound to the surface, the temperature for subsequent material growth is restricted to avoid desorption. For example, dielectrics grown on physisorbed seeding molecules suffer from a poor density and impurities, resulting from unpurged precursor gases and growth byproducts[7,14]. Besides

[1]Katholieke Universiteit, Leuven 3000, Belgium. [2]imec, Leuven 3001, Belgium. [3]ASM, Leuven 3001, Belgium. ✉e-mail: Pieter-Jan.Wyndaele@imec.be

single physisorbed molecules, seeding layers have been widely explored owing to their higher thermal stability[7,15]. Different types of seeding layers e.g., polymer-[16], organic-[17] and metal oxide-based[18], have been demonstrated to result in uniform material growth. For example, a sub nm $SiO_2$ seeding layer enables good dielectric growth, but contamination and poor interface quality give rise to charge trapping at the $MX_2$/seeding layer interface, degrading performances[2,15]. Therefore, the ideal seeding layer has a self-passivated surface to establish a vdW interface, not degrading the desired $MX_2$ properties.

Another popular member of the 2D family is graphene (Gr), but its utilization as seeding layer simply defers the deposition problem to the next self-passivated surface[19]. However, great effort has been put into covalently functionalizing graphene as reported by De Feyter and colleagues[8,20,21]. Using functionalized graphene as a sacrificial seeding layer has been demonstrated in the past[22]. Nourbakhsh et al. selectively functionalized the upper layer of a bilayer graphene stack using a pulsed oxygen plasma, after which an $Al_2O_3$ dielectric was grown via ALD resulting in a high performance, top-gated graphene field-effect transistors (FETs). However, the graphene oxide (GrO) contribution to the total gate capacitance can become significant as it scales with the O/C ratio[23]. Therefore, a GrO seeding layer can only be utilized for application tolerating its quantum capacitance, for which a large array of logic gates and integrated circuits is still envisioned[24], as well as sensor focused applications[25].

A seeding layer provides another advantage in forming a physical barrier that limits ambient exposure of the $MX_2$ layer, which is prone to aging effects i.e., spontaneous oxidation upon ambient exposure[26,27]. An encapsulation-based method is, however, typically considered suboptimal as it complicates further processing or leads to damage upon removal[28]. However, this can be circumvented by integrating the passivation layer e.g., as a seeding layer for subsequent material growth.

In this study, GrO is used as a sacrificial seeding layer to passivate and enable uniform, high-$\kappa$ dielectric growth on monolayer $WS_2$. Our approach involves 3 main steps (1) graphene transfer; (2) graphene cleaning i.e., removal of transfer polymeric residues by combining solvent- and hydrogen downstream plasma source (DPS) treatments; (3) graphene functionalization via a dry UV/$O_3$ oxidation process. Subsequently, a $HfO_2$ dielectric is deposited via ALD on the GrO seeding layer. The paper consists of two sections. The first part focuses on the characterization of the different process steps. This is demonstrated for graphene transferred onto $SiO_2$ to simplify sample preparation. The second part applies the learnings of the first to a Gr/$WS_2$ stack, demonstrating proof of concept. A graphene-based nucleation- / passivation layer offers the flexibility to adapt the surface functionalization to the precursor gas chemistry, enabling alternative material growth (other than dielectrics) while maintaining a high-quality interface.

## Results and Discussion

### Graphene cleaning via solvent- and hydrogen downstream plasma source treatments

Chemical vapor deposition (CVD) is widely used to produce high quality graphene at scale[29], but requires graphene to be transferred from the growth- to target substrate. Detailed descriptions of both the growth and transfer processes can be found in the method section. A sacrificial polymer film i.e., poly(methyl methacrylate) (PMMA) is spin-coated directly on graphene to preserve its structural integrity during transfer. Afterwards, a solvent treatment is carried out to remove the bulk polymer material (see methods). Figure 1a–d shows atomic force microscopic (AFM) images of graphene's surface before and after AFM tip cleaning. Here, the AFM tip acts like a brush that shoves physisorbed molecules towards the scan edges, after which the change in topography can be used to assess layer thickness[30]. The contamination build-up noted in Fig. 1d corresponds to PMMA transfer residues, which are difficult to remove due to the $\pi$-$\pi$ stacking between the polymer chains and graphene's conjugated network[31,32]. To weaken this interaction, polymer degradation via radiative- or thermal treatments has been explored since the higher solubility of the smaller fragments makes them easier to remove[33]. Conversely, radicals produced in these processes may also chemically react with graphene defects which complicates the cleaning process[34].

Hydrogen-based downstream plasma treatments have been explored as alternative cleaning methods on account of their scalability[31,35–37]. In this

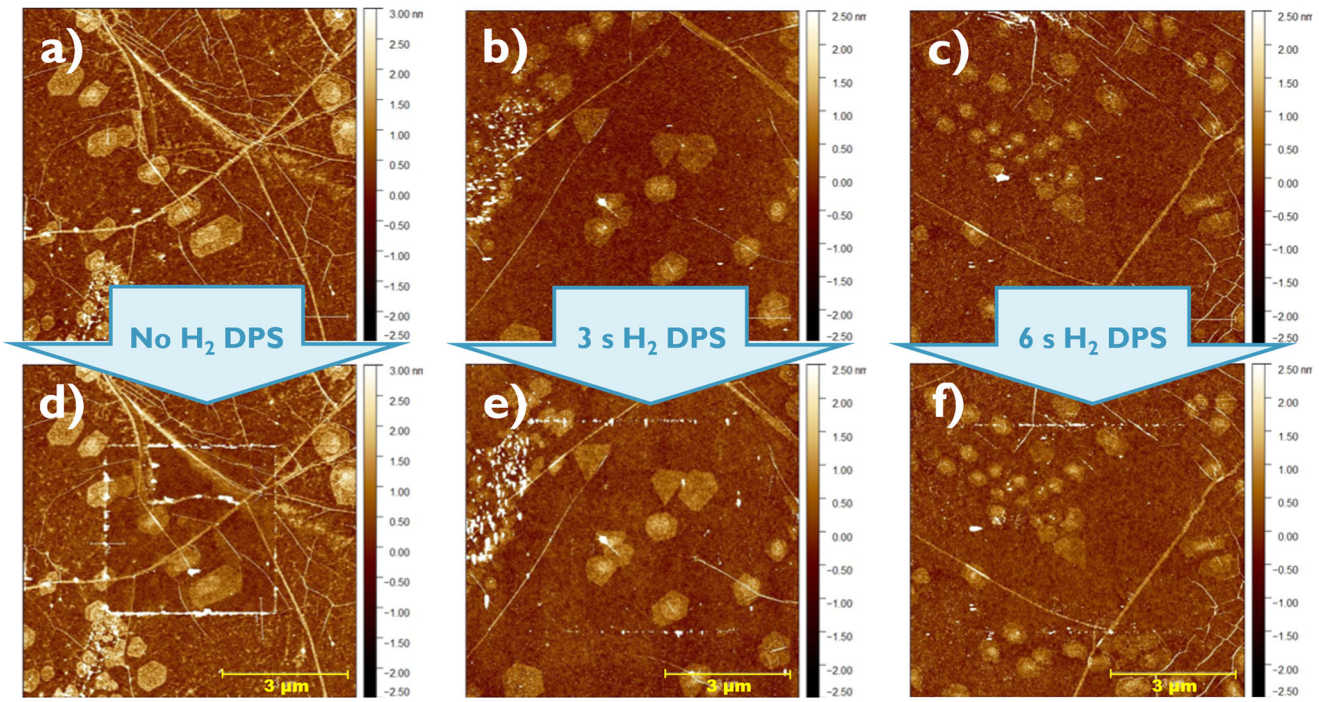


**Fig. 1 | PMMA transfer residue cleaning via $H_2$ Downstream Plasma Source (DPS). a**, **d** AFM images after tip cleaning of solvent treated graphene without plasma exposure, where PMMA residues pile up on the scan edge (4 µm$^2$) when brushed away by the AFM tip. **b**, **e** No PMMA pile-up is noted for graphene treated with a solvent and 3- or **c**, **f** 6 s $H_2$ DPS exposure.

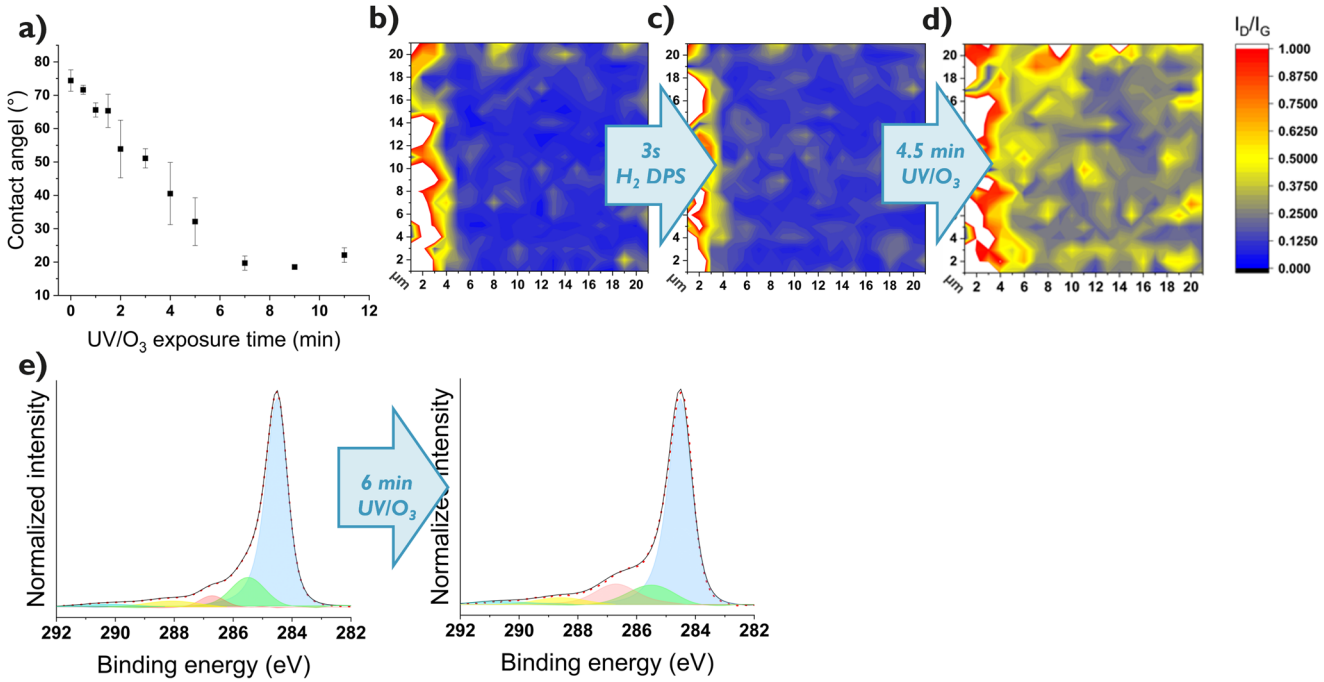


**Fig. 2 | Dry UV/$O_3$ functionalization of graphene. a** Effect of UV/$O_3$ oxidation on the wettability of cleaned graphene, showing an increase in hydrophilicity. **b** Raman mapping before, **c** after 3 s $H_2$ DPS treatment and **d** after 4.5 min UV/$O_3$ exposure, showing a significant increase in $I_D/I_G$ ratio i.e., graphene functionalization. **e** Normalized XPS C*1s* spectra measured before and after 6 min UV/$O_3$ exposure showing an increase in shoulder peak ~286.5 eV i.e., C-O single bond, basal plane functionalities.

configuration, a baffle separates the sample from the plasma discharge which prevents ion bombardment and only allows diffusion of thermal radicals to the sample surface. The hydrogen radicals induce a scission of the polymer chain, leading to smaller and volatile etch products. Details on the etching mechanism of PMMA by hydrogen radicals are discussed elsewhere[38]. Figure 1b–e shows tip-cleaned AFM images after solvent treatment and 3 s $H_2$ DPS exposure, revealing no significant contamination build-up at the scan edges. Extending the $H_2$ DPS exposure to 6 s shows a similar contamination build-up (Fig. 1c–f), suggesting the marginal amount of residues still present may be inorganic in nature or originate from post-cleaning ambient exposure. Note some spots are present in all AFM tip-cleaned areas, which correspond to graphene bi- or multilayer islands as discussed in the Supplementary information (Supplementary Fig. 1).

The hydrogen radicals may also interact with the graphene layer itself. Despiau-Pujo et al. predicted that atomic hydrogen species can penetrate, adsorb or be reflected from the graphene surface depending on their energy[39]. Raman characterization assesses graphene surface modifications resulting from the $H_2$ DPS treatment. Figure 2b, c shows Raman mappings of solvent treated graphene before and after 3 s $H_2$ DPS exposure, respectively. The white mark on the left is part of a reference scratch used for consecutive measurements. The color scale corresponds to an $I_D/I_G$ ratio, typically used to assess graphene quality. An increase in D (~1350 $cm^{-1}$) to G peak (~1590 $cm^{-1}$) ratio suggest a larger defectivity, since the D phonon mode requires a structural defect for its activation[40]. Some growth-related non-uniformity can be observed in Fig. 2b, which is to be expected given the large mapping scale (20 $\mu m^2$). A small increase in $I_D/I_G$ ratio is noted after $H_2$ DPS exposure and additional quantitative analysis is provided in the Supplementary information (Supplementary Fig. 2). The slight $I_D/I_G$ increase is attributed to limited hydrogenation, since no macroscopic defects are present in the AFM images (Fig. 1) after plasma exposure.

Plasma hydrogenation of graphene has been reported, leading to C-H bond formation that changes carbon's $sp^2$- to a $sp^3$ hybridization (D peak increase) and breaking of the C=C translational symmetry (G peak decrease)[41]. Even though plasma hydrogenation is known to be reversible e.g., via thermal annealing[41], its minor impact is tolerated since graphene's conjugated network will be sacrificed anyway during subsequent UV/$O_3$ oxidation. Hereafter, a solvent- and 3 s $H_2$ DPS treated layer will be referred to as cleaned graphene.

### Graphene functionalization via dry UV/$O_3$ oxidation

The cleaned graphene is subsequently functionalized via dry UV/$O_3$ oxidation, forming the sacrificial seeding layer. This method is known to be reversible upon UV irradiation[42], demonstrating the gentle nature of the oxidation process. A soft functionalization is essential since damaging the graphene lattice would expose the underlying $WS_2$ monolayer during further processing. On the one hand, the graphene layer requires sufficient oxidation to generate adequate carbon-oxygen functionalities. On the other hand, the carbon lattice should not be physically damaged due to excessive UV/$O_3$ exposure e.g., UV light induced heating[42] to also retain its passivation properties. Establishing this delicate balance requires a thorough characterization of the UV/$O_3$ treatment.

Figure 2a shows the effect of UV/$O_3$ oxidation on graphene's wettability. The contact angle gradually decreases over 6 min, after which a constant angle of ~20° is reached. The hydrophobicity decrease is explained by the polar carbon-oxygen functionalities formed, for which the reaction mechanism is reported elsewhere[43]. However, a contact angle of 20° is comparable to the wettability measured for $SiO_2$ substrate after 6 min UV/$O_3$ (Supplementary information, Supplementary Fig. 3). Consequently, the drop in hydrophobicity may be caused by graphene oxidation or $SiO_2$ substrate exposure, suggesting graphene etching.

Raman mappings are recorded before and after 4.5 min UV/$O_3$ to verify the presence of graphene (oxide), shown in Fig. 2c, d, as well as standard (1D) Raman spectroscopy after 7.5 min—see Fig. 5b. Overall, the $I_D/I_G$ increases significantly after UV/$O_3$ exposure, confirming graphene oxidization. The dismissal of graphene etching is based on the large remaining intensity of both the D and G peaks even after 7.5 min UV/$O_3$ indicating that, although oxidized, graphene remains present on the $SiO_2$ substrate.

Additionally, X-ray photoelectron spectroscopic (XPS) analysis monitors the change in graphene's surface state i.e., the type of chemical

group formation. Figure 2e shows normalized XPS spectra of the C*1s* core level of graphene before and after 6 min UV/$O_3$, with Table 1 summarizing the peaks deconvolution. No significant spectral changes are noted ~287.5 and ~288.9 eV, associated with double bond carbon-oxygen functionalities (i.e., carbonyl and carboxyl groups, respectively)[44–46]. These double bond functionalities require σ-electrons of the carbon-carbon bonds i.e., the graphene lattice itself to be sacrificed, whereupon it would lose its passivation properties. However, there is an increase in peak intensity ~ 286.5 eV, associated with single bond carbon-oxygen functionalities (i.e., epoxy- and hydroxyl groups), created by sacrificing the $\pi$-electrons from graphene's conjugated network[46,47]. Exposing graphene to a dry UV/$O_3$ exposure thus predominantly forms carbon-oxygen single-bond i.e., basal plane functionalities.

### Evaluation $H_2$ DPS cleaning and UV/$O_3$ oxidation via back-gated GFET

A graphene field effect transistor (GFET) is exposed to $H_2$ DPS and dry UV/$O_3$ treatments to evaluate their effects on graphene's transport properties. Details on GFET fabrication are summarized in the method section. Figure 3a illustrates the back-gated, 4-probe GFET, whose dimensions are summarized in Table 2. Additional optical images and Raman spectra are provided in the Supplementary information (Supplementary Fig. 4). Figure 3b, c shows I-V and resistance curves before and after $H_2$ DPS cleaning and 7.5 min UV/$O_3$ oxidation. After transfer, characteristic transport is noted but the Dirac point ($V_k$) is heavily shifted. The $V_k$ shift towards positive gate voltage results from p-doping caused by the PMMA residues shown in Fig. 1a–d[48–51].

After $H_2$ DPS cleaning, $V_k$ shifts towards 0-point voltage, again demonstrating the effectiveness of the cleaning process. Table 2 summarizes the GFET figures of merit, extracted based on the work of de la ref. 52 and is explained in more detail in the Supplementary information (Supplementary Fig. 5). There is a small loss in current after $H_2$ DPS cleaning ($I_{on}/I_{off}$ : 5.9 → 5.4), while both the electron- ($\mu_{electron}$) and hole mobilities ($\mu_{hole}$) increase albeit asymmetrical ($\mu_{electron}$ : 602.7 → 1107.1 $cm^2V^{-1}s^{-1}$, $\mu_{hole}$ : 1890.0 → 2020.5 $cm^2V^{-1}s^{-1}$). These 3 observations are explained by considering the following 3 effects: (1) The small loss in current is attributed to limited graphene hydrogenation, as demonstrated in Fig. 2b, c and in line with the results of ref. 53. (2) The $\mu_{electron}$ and $\mu_{hole}$ enhancement is explained by the removal of the PMMA residues, which otherwise act as scattering sites in accordance with ref. 54. (3) Finally, D.B. Farmer et al. observed that graphene p-doping via diazonium functionalization does not drastically change the hole conductance, while the electron conductance was heavily suppressed due to a neutrality point misalignment caused by the channel doping[55]. Conversely, in this study, $H_2$ DPS cleaning removes the neutral point misalignment caused by the p-dopant i.e., PMMA residues, which results in the asymmetric, larger increase in $\mu_{electron}$ compared to $\mu_{hole}$.

After 7.5 min UV/$O_3$, graphene's conductance is suppressed to the nA range. The drop in current results from the sacrifice of graphene's π-con-

**Table 1 | Deconvolution peaks of XPS C*1s* spectra**

| | Graphene | | | Graphene + 6 min UV/O3 | | |
|---|---|---|---|---|---|---|
| Peak | Position (eV) | FWHM (eV) | At conc (%) | Position (eV) | FWHM (eV) | At conc (%) |
| C=C | 284.4 | 0.8 | 66.2 | 284.4 | 0.9 | 64.8 |
| C–C | 285.3 | 1.3 | 21.3 | 285.3 | 1.9 | 17.3 |
| C–O | 286.5 | 1.0 | 5.1 | 286.4 | 1.6 | 10.4 |
| C=O | 287.5 | 2.1 | 3.1 | 287.5 | 2.0 | 3.6 |
| O–C=O | 288.9 | 2.0 | 4.3 | 289.0 | 2.0 | 4.0 |

**Table 2 | Summary of GFET device dimensions and figures of merit**

| Device Characteristics | | Figures of merit | | |
|---|---|---|---|---|
| Parameter | Numeric Value | $H_2$ DPS | Before | After |
| $L_{4P}$ | 20 µm | $I_{ON}/I_{OFF}$ (-19$V_{overdrive}$) | 5.8 | 5.4 |
| $W_{CHANNEL}$ | 20 µm | $\mu_e$ ($cm^2$ $V^{-1}s^{-1}$) | 602.7 | 1107.1 |
| $L_{CHANNEL}$ | 50 µm | $\mu_h$ ($cm^2V^{-1}s^{-1}$) | 1890.0 | 2020.5 |
| $V_{DS}$ | 1.0 V | $V_k$ (V) | 18 | 0 |

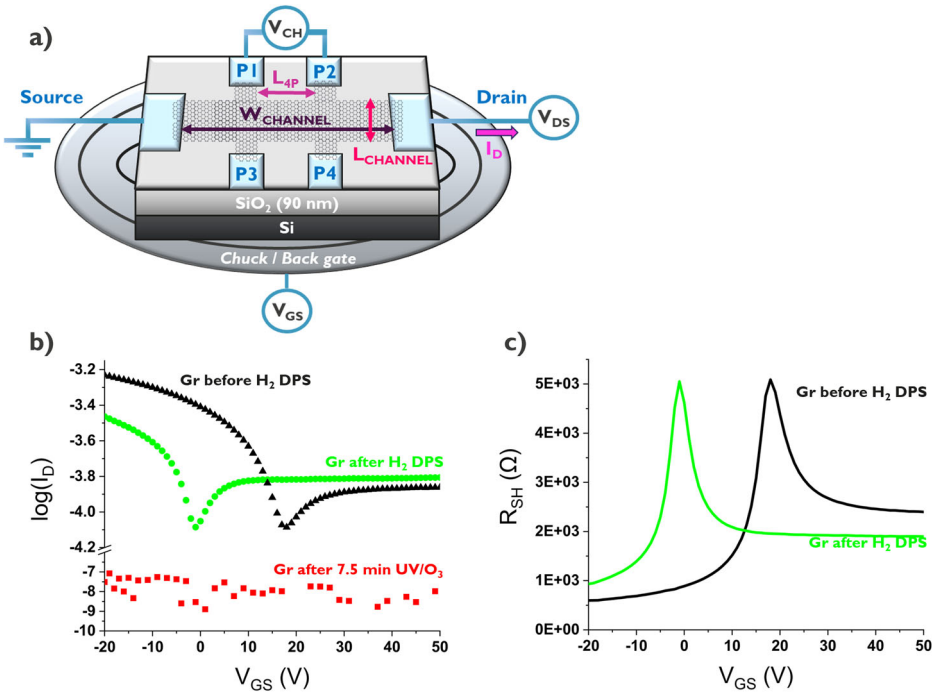


**Fig. 3 | Evaluation of graphene's transport properties after $H_2$ DPS cleaning and UV/$O_3$ oxidation. a** Illustration 4-probe GFET. **b** $I_D$-$V_{GS}$ characteristics of backgated GFET before- and after $H_2$ DPS exposure, showing a shift in $V_k$ which results from PMMA residue removal. After 7.5 min UV/$O_3$, graphene's conductance is significantly suppressed. **c** Graphene's sheet resistance as a function of $V_{GS}$ before- and after $H_2$ DPS exposure.

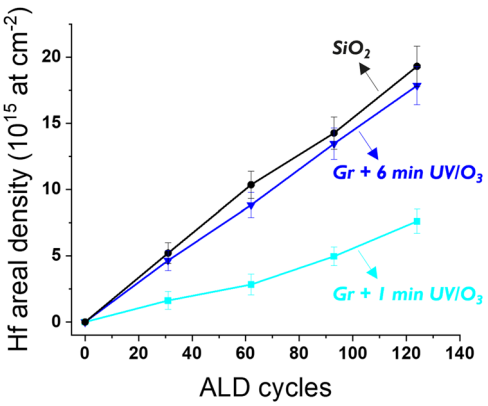


**Fig. 4 | $HfO_2$ ALD on graphene oxide seeding layers.** Hf areal density measured by RBS showing a similar growth on 6 min UV/$O_3$ functionalized graphene when benchmarked against a $SiO_2$ i.e., well-functionalized substrate.

jugated network to form the basal plane functionalities as evidenced by Fig. 2e. The evolution of graphene's transport properties substantiates a clean graphene surface post $H_2$ DPS cleaning. Subsequent UV/$O_3$ oxidation functionalizes the basal plane, converting it into a seeding layer.

### $HfO_2$ ALD on GrO/$SiO_2$

A $HfO_2$ ALD process is applied to the UV/$O_3$ functionalized graphene to test the seeding layer growth characteristics. Figure 4 shows the Hf areal density measured by Rutherford backscattering spectrometry (RBS) after ALD on graphene layers functionalized with various UV/$O_3$ exposure times. 1 min UV/$O_3$ leads to a non-linear growth, indicating a growth delay. Extending the UV/$O_3$ exposure to 6 min results in linear growth and a significant increase in overall Hf deposition, demonstrating the enhanced surface functionalization. The growth enhancement is also confirmed by scanning electron microscopic images (Supplementary information, Supplementary Fig. 6), showing graphene exposed to 1 min UV/$O_3$ is only decorated by $HfO_2$ island after 124 ALD cycles, whereas 6 min UV/$O_3$ results in more uniform growth and layer closure.

In addition, the $HfO_2$ growth is benchmarked against $SiO_2$, representing a model substrate with a well-functionalized surface. The Hf density measured on $SiO_2$ is comparable to 6 min UV/$O_3$ exposed graphene, demonstrating that good dielectric growth can be achieved after adequate UV/$O_3$ functionalization.

### Fabrication and characterization of 2D Gr/$WS_2$ heterostack

Detailed descriptions of the monolayer $WS_2$/graphene growth and transfer processes can be found in the method section. Extensive characterization of the Gr/$WS_2$ heterostack is presented in the Supplementary information which includes AFM tip cleaning and Raman spectroscopy, demonstrating a clean, high-quality graphene layer (Supplementary Fig. 7). In addition, the high-quality Gr/$WS_2$ vdW interface is evidenced by Raman phonon and Photoluminescence (PL) quenching resulting from the interlayer coupling (Supplementary Fig. 7). Lastly, the graphene and $WS_2$ monolayer thicknesses are confirmed via Raman- and PL characterization (Supplementary Fig. 8).

### Substrate dependency of selective graphene oxidation towards underlying $WS_2$ monolayer

The Gr/$WS_2$ heterostack is exposed to a dry UV/$O_3$ treatment to functionalize graphene's basal plane as demonstrated in the first part of the paper. Figure 5 shows Raman spectra of UV/$O_3$ exposed graphene transferred on (a) monolayer $WS_2$ and (b) 90 nm $SiO_2$. For Gr/$SiO_2$, the D peak significantly increases after 7.5 min UV/$O_3$ and longer exposure leads to Raman quenching. For Gr/$WS_2$, a similar D peak increase requires up to 30 min of UV/$O_3$ exposure. The rate of graphene oxidation appears to be substrate dependent and is a peculiar phenomenon that impacts the process flow. Authors theorize it results from UV light-induced charge transfer between the graphene and $WS_2$ monolayer. This hypothesis is based on the interplay of the following two phenomena.

First, the reaction mechanism during UV/$O_3$ oxidation is discussed. Atomic oxygen is generated by exposing oxygen gas to UV light ($\lambda$ = 184.9 nm), resulting in ozone formation. The ozone molecule dissociates ($\lambda$ = 253.7 nm) into an oxygen molecule and atomic oxygen. The atomic oxygen diffuses to the graphene layer where it adsorbs in a 'bridge' position i.e., in between two adjacent carbon atoms due to the favorable hybridization of the 2p orbitals of the carbon and oxygen atoms[56]. In other words, the oxygen atom chemisorbs onto graphene by consuming π-electrons of two carbon atoms to satisfy its octet configuration, forming an epoxide group[42]. Importantly, this reaction does not consume any electrons making up the carbon σ-bonds and thus leaves the graphene lattice intact. Consequently, a dry UV/$O_3$ exposure results predominantly in epoxy functionalization of graphene's basal plane, both theoretically[56–58] and experimentally verified by the XPS results shown in Fig. 2e.

Second, the Gr/$WS_2$ band structure is considered and how it changes upon UV light exposure. In the ground state, the Gr/$WS_2$ band structure is simply a superposition of the individual bands due to their weak vdW interactions, without substantial charge redistribution[59,60]. However, ultrafast charge transfer can occur upon excitation e.g., via electron pump or UV light exposure. This charge transfer is demonstrated by the PL quenching of the $WS_2$ monolayer before and after graphene capping, enabled by the high quality vdW interface (Supplementary information, Supplementary Fig. 7). During charge transfer from the $WS_2$ monolayer to graphene, holes in the $WS_2$ valence band maximum (VBM) tunnel faster than electrons in the conduction band minimum (CBM) due to a stronger coupling of the VBM with graphene's acceptor states[59]. When excited continuously, the difference in electron and hole diffusion rates leads to a positive charge build-up in the graphene layer[59].

Finally, the graphene oxidation substrate dependency is summarized (Fig. 5). UV light generates atomic oxygen, but also excites carriers in the $WS_2$ monolayer. Constant UV exposure continuously generates electron-hole pairs where $WS_{2,\ holes}$ tunnel faster than $WS_{2,\ electrons}$, leading to a positive charge build-up in graphene that lowers the effective electron density. Consequently, its π-electrons are less prone to bind atomic oxygen i.e., slows down the oxidation process. As a result, graphene oxidation requires longer UV/$O_3$ exposure when transferred on $WS_2$ compared to $SiO_2$, where no interlayer charge transfer takes place. XPS characterization of the C*1s* core level of UV/$O_3$ exposed Gr/$WS_2$ is carried out to verify the substrate dependency (Supplementary information, Supplementary Fig. 10). However, no significant changes in peaks contributions are noted, possibly due to interference from the extra signal originating from $WS_2$ monolayer, lowering the overall measurement sensitivity.

The dry UV/$O_3$ oxidation functionalizes graphene but should not affect the underlying $WS_2$ monolayer. PL spectroscopy is widely used to monitor changes in $MX_2$ monolayers on account of its extreme sensitivity[61], but cannot be utilized in this case due to interlayer quenching as explained in the Supplementary information (Supplementary Fig. 7). Raman spectroscopy is another optical technique used to detect $WS_2$ modifications[62], but which is not prone to interlayer quenching. Figure 6a shows the Raman response of $WS_2$ monolayer after different UV/$O_3$ exposures with- (a) and without graphene capping (b). Graphene capped $WS_2$ shows no loss in Raman signal after graphene cleaning nor over 30 min UV/$O_3$ exposure, while uncapped $WS_2$ shows significant Raman quenching after 7.5 min UV/$O_3$. The loss in Raman response suggests UV/$O_3$ induced layer damage[63], which is prevented after graphene capping. XPS is carried out to monitor changes in $W_{metal}$ to $W_{oxide}$ chemical states resulting from the UV/$O_3$ oxidative treatment. Figure 6c shows the W*4f* core level of graphene capped- and uncapped $WS_2$ treated for various UV/$O_3$ exposure times. The deconvoluted spectra are included in the Supplementary information (Supplementary Figs. 11 and 12) and a detailed description of the deconvolution method is provided in the method section. The stacked plot shown

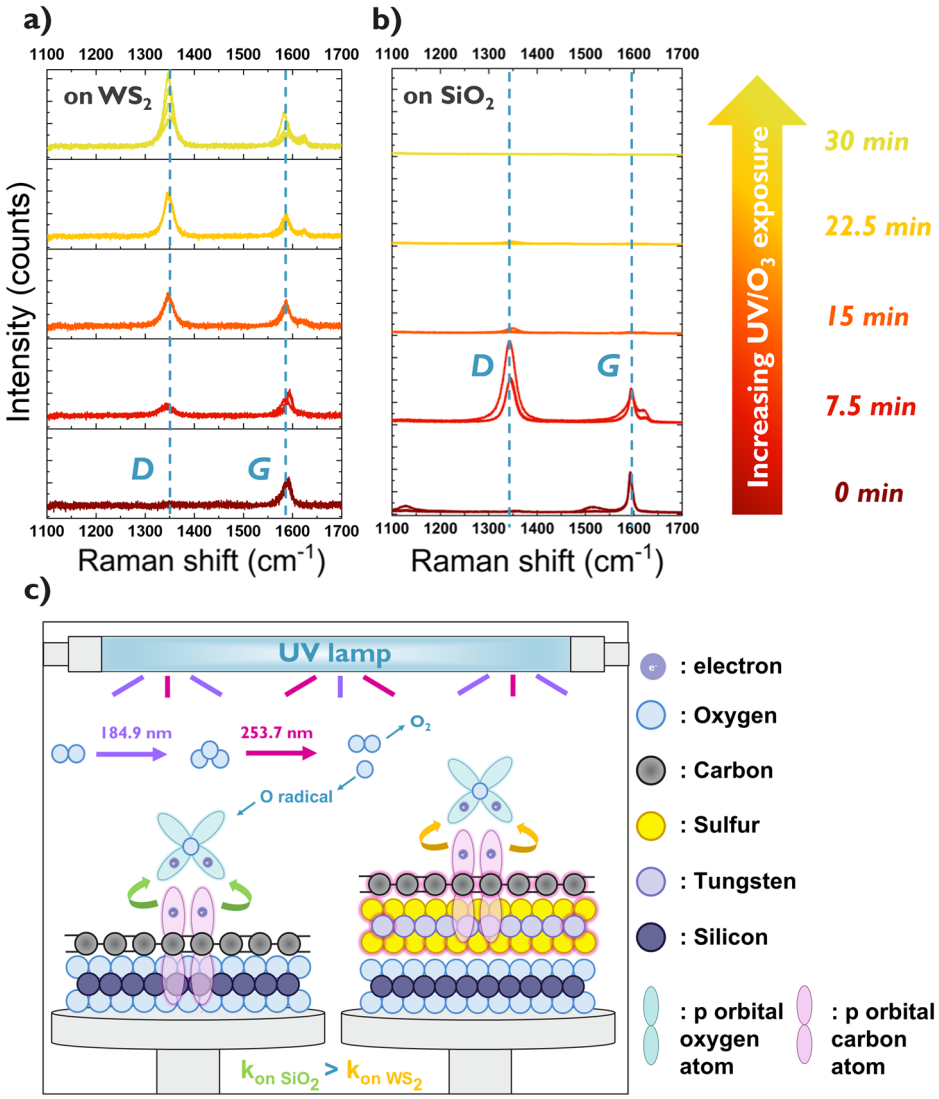


**Fig. 5 | Graphene dry UV/$O_3$ oxidation substrate dependency.** Stacked Raman spectra of UV/$O_3$ exposed graphene **a** on $WS_2$ showing significant modifications after 30 min, whereas **b** when transferred on $SiO_2$ only 7.5 min suffice. **c** Authors explain this substrate dependency on account of UV-light induced, ultrafast charge transfer between the graphene and $WS_2$ monolayer, lowering graphene's electron density and resulting in a slower UV/$O_3$ oxidation rate compared to a $SiO_2$ substrate.

in Fig. 6c summarizes the $W_{metal}$ and $W_{oxide}$ peak contributions, which show no significant changes after graphene capping, $H_2$ DPS cleaning and 7.5 min UV/$O_3$ oxidation compared to the as grown $WS_2$ monolayer. Over 15–30 min UV/$O_3$, a gradual, small increase in $W_{oxide}$ contribution is observed, in contrast to uncapped $WS_2$ for which a significant increase in $W_{oxide}$ contribution is noted after 7.5 min. In comparison, $W_{oxide}/W_{total}$ after 30 min UV/$O_3$ is 25.2% / 80.7% for graphene capped/ -uncapped $WS_2$. These results confirm the loss in Raman signal in Fig. 6b is caused by $WS_2$ oxidation, which is prevented after graphene capping that maintains its passivation properties throughout the oxidation process. The limited $W_{oxide}$ increase is attributed to limited imperfections in the graphene layer, anticipated from the large-scale ($2.5 \times 2.5$ $cm^2$) growth and transfer processes (methods). These imperfections e.g., point-defects and grain boundaries readily oxidize compared to the basal plane and do not passivate during extended UV/$O_3$ exposure.

In addition, uncapped $WS_2$ exposed to ambient i.e., 24 h per day light exposure in a controlled environment with 40.2% relative humidity & 19.1% $O_2$ gas concentration, shows a similar increase in $W_{oxide}/W_{total}$ of 81.8% compared to uncapped $WS_2$ treated with 7.5 min UV/$O_3$ (Supplementary information, Supplementary Figs. 13 and 14). Therefore, it is reasonable to assume that graphene capping not only protects the underlying $WS_2$ monolayer in a strong oxidative environment e.g., dry UV/$O_3$ exposure, but also mitigates spontaneous ambient oxidation i.e., aging effects[26,27].

### $HfO_2$ ALD study on GrO/$WS_2$

A $HfO_2$ ALD study is carried out on GrO/$WS_2$ to evaluate the GrO seeding layer's growth characteristics. Figure 7a shows the Hf areal density measured by RBS after ALD on uncapped- and graphene capped $WS_2$ exposed to 30 min UV/$O_3$. A substantially enhanced Hf deposition is noted on GrO/$WS_2$ compared to direct deposition on $WS_2$, for which there is a strong nucleation delay. Benchmarking the $HfO_2$ growth on GrO/$WS_2$ against $SiO_2$ reveals similar trends, again demonstrating the GrO surface is well-functionalized and results in good material deposition.

The $HfO_2$ layer roughness is measured via AFM to examine surface coverage and layer closure throughout the ALD process (Supplementary information, Supplementary Fig. 15). Figure 7b plots the $HfO_2$ layer roughness after ALD on GrO capped- and uncapped $WS_2$. Direct growth on $WS_2$ shows a gradual increase in layer roughness which stabilizes only after 248 cycles ~5–6 nm, while a constant roughness of ~1–1.5 nm is measured on GrO/$WS_2$. The large increase in roughness together with nucleation delay demonstrate the poor, island-like growth when done directly on the $WS_2$ monolayer, similar to the trends observed in Fig. 4. The low, constant roughness of the $HfO_2$ layer grown on GrO/$WS_2$ demonstrates uniform material deposition and fast layer closure even in the early stages of the ALD process. Additionally, scanning transmission electron microscopic images are provided in the Supplementary information (Supplementary Fig. 16) that show a smoother $HfO_2$ layer on GrO/$WS_2$ compared to direct growth on

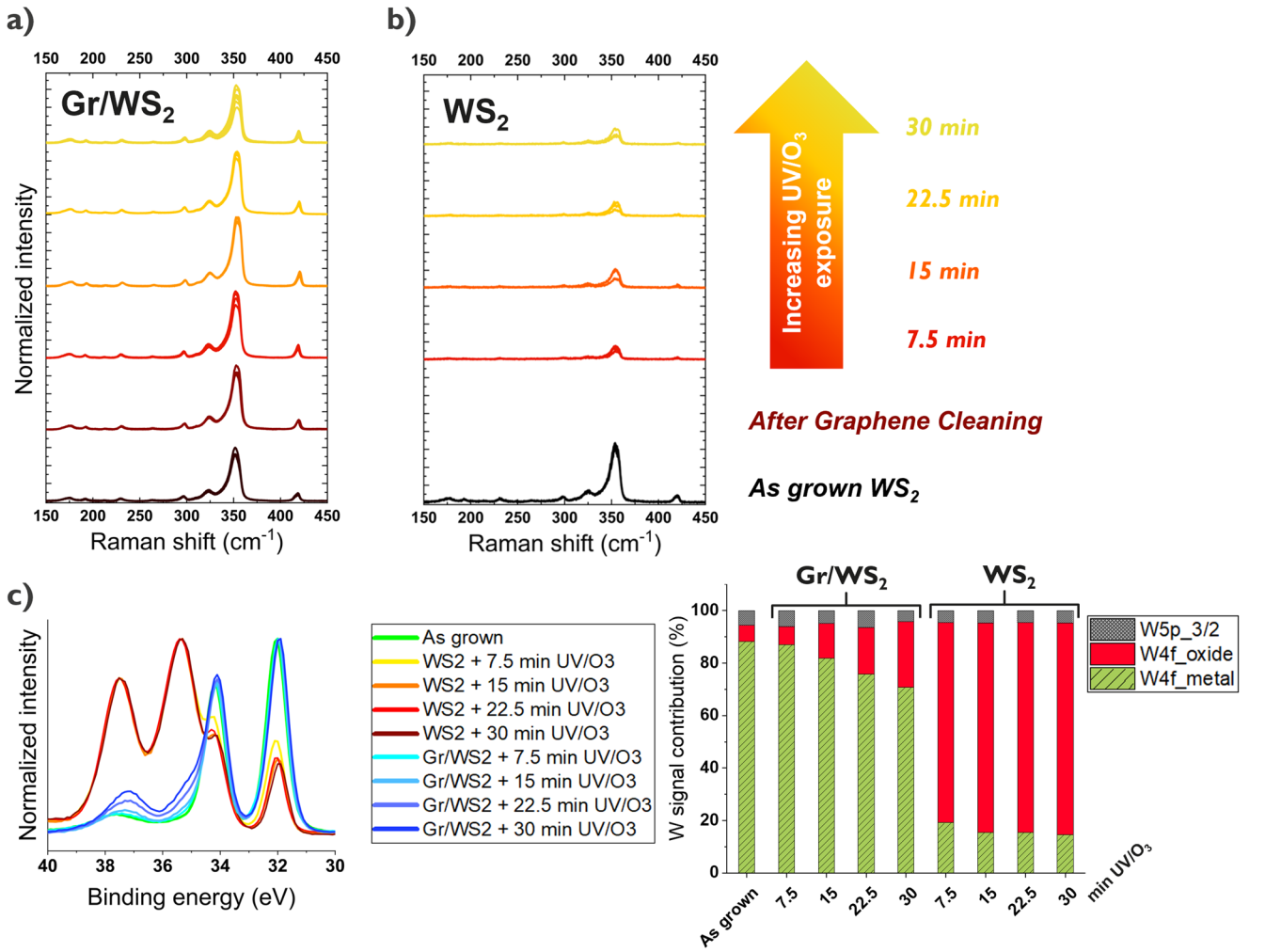


**Fig. 6 | Passivation properties of the graphene oxide seeding layer.** Raman spectra of UV/$O_3$ exposed $WS_2$ (normalized w.r.t Si 520 $cm^{-1}$) **a** with graphene capping showing no loss in signal over 30 min UV/$O_3$, whereas **b** uncapped $WS_2$ shows signal quenching after 7.5 min. **c** Normalized XPS W*4f* spectra, showing graphene passivated $WS_2$ exhibits limited increase in $W_{oxide}$ peak contributions i.e., layer damage compared to uncapped $WS_2$.

**Fig. 7 | $HfO_2$ ALD on GrO/$WS_2$.** **a** Hf areal density measured by RBS showing a similar growth for 30 min UV/$O_3$ functionalized GrO/$WS_2$ compared to SiO2 i.e., well-functionalized substrate. **b** $HfO_2$ layer roughness extracted from AFM images revealing a growth delay for uncapped $WS_2$, whereas the lower and constant $HfO_2$ layer roughness on GrO/$WS_2$ demonstrates uniform growth and fast layer closure.

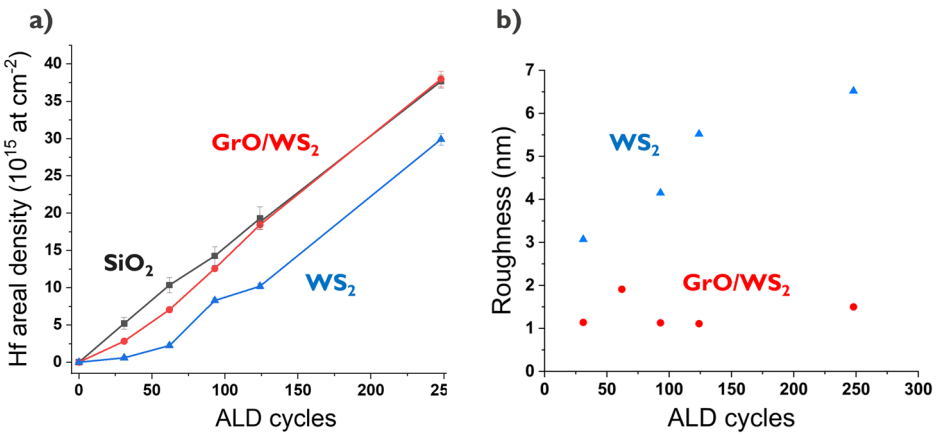


$WS_2$, confirming the GrO seeding layer leads to enhanced material deposition.

In summary, we present a flexible approach to facilitate the nucleation and $HfO_2$ growth on monolayer $WS_2$. Our method utilizes a graphene oxide seeding layer, serving a dual purpose (1) as passivation layer, allowing for a perfect van der Waals interface and (2) as seeding layer, for which the surface chemistry can be tailored to enable other types of material growth.

After transfer, a two-step cleaning process (solvent + $H_2$ downstream plasma treatments) removes polymeric transfer residues from the graphene surface. The large-scale hydrogen plasma cleaning is highly selective towards graphene, verified by GFET analysis. The cleaned graphene is then functionalized selectively towards the underlying $WS_2$ via dry UV/$O_3$ oxidation, during which basal plane functionalities are formed that leave the carbon lattice and its passivation properties intact. Interestingly, the

oxidation rate is lower when graphene is transferred on $WS_2$ compared to $SiO_2$. This substrate dependency possibly results from ultrafast charge transfer via the interlayer coupling between graphene and the $WS_2$ monolayer. Graphene capping passivates the underlying $WS_2$ during oxidative $UV/O_3$ exposure and, therefore, is expected to also protect against aging effects.

The carbon-oxygen functionalities serve as nucleation sites in a subsequent ALD process, significantly enhancing $HfO_2$ growth compared to direct deposition on $WS_2$ and a similar deposition when benchmarked against a well-functionalized surface in $SiO_2$. Moreover, the constant $HfO_2$ roughness measured throughout the ALD process indicates uniform deposition and fast layer closure. Our methodology is expected to be generally applicable to different 2D TMDC flavors since the different treatments are applied to the sacrificial graphene (oxide) layer and not directly to the $MX_2$ film. Ultimately, a graphene-based seeding layer offers adaptability i.e., tailored functionalization to enable alternative material growth, while preserving a van der Waals interface to prevent degradation of the 2D TMDC properties.

## Methods

### $WS_2$ growth

The $WS_2$ monolayer was grown via metal organic chemical vapor deposition on 300 mm silicon wafers covered with a 90 nm thermal oxide. At first, the wafer was heated under high-purity $N_2/H_2$ until a chamber temperature of 750 °C was reached. The growth started with a nucleation step, where $W(CO)_6$ (partial pressure ~$9 \times 10^{-3}$ Torr) and $H_2S$ gases were introduced (precursor partial pressures ratio $H_2S/W(CO)_6 = 5 \times 10^3$) for 10 min at 750 °C at a chamber pressure of 150 Torr. Next, the chamber temperature was increased to 900 °C and the chamber pressure lowered to 20 Torr to enhance lateral growth and promote layer closure.

### Graphene growth and transfer

Two types of graphene were used in this study: commercially available graphene produced by Graphenea and graphene produced at imec, which were used for the first- and second part of the paper respectively.

Graphene growth at Graphenea was performed in a Black Magic Pro 2 × 8" CVD furnace from Aixtron Ltd on a copper foil. A $H_2$ pre-annealing was done at 900 °C, after which the temperature was raised to 1000 °C and methane gas introduced in the chamber until the chamber pressure reached 25 mbar. After 30 min, the methane was evacuated, the growth chamber purged and cooled down to room temperature in Ar. Next, the malleable Gr/Cu foil catalyst was covered with a PMMA coating and then laminated with an adhesive polymer carrier to provide a more rigid support during transfer. The catalyst was etched via a wet etching process performed in borosilicate glass tanks using $FeCl_3$ as an etchant. Several consecutive ultra-pure deionized $H_2O$ and acidic rinses of diluted solutions of hydrochloric acid (37%) were used to wash the $FeCl_3$ etchant and minimize the metal traces concentration, after which the graphene was dried via a $N_2$ flow. The graphene layer was then laminated via a dry method onto the $SiO_2$ target wafer. Namely, the adhesive carrier/PMMA/graphene stack was roll-laminated at a pressure above 1 bar at a temperature of 150 °C, after which the carrier polymer was removed leaving PMMA/graphene layers behind on the $SiO_2$ wafer. At imec, the 300 mm wafers were manually cleaved into coupons for further processing.

At imec, graphene was grown via CVD in a Black Magic BM6 from Aixtron Ltd on a 2.5 × 2.5 $cm^2$ Platinum foil[64], which was cleaned by acetone-, short oxygen plasma- and piranha solvent treatments. The growth chamber was gradually heated up to 1170 °C in a $H_2$-rich environment at a chamber pressure of 750 mbar, after which a waiting time of 6 min was set to ensure the Pt foil was properly annealed. Next, a $H_2/CH_4$ gas mixture (800/4 sccm) was introduced into the chamber for 40 min. Subsequently, the chamber was cooled down and when the chamber temperature dropped below 700 °C, the $CH_4$ precursor was switched off. The $H_2$ supply was turned off only when the temperature dropped below 150 °C. The rich-$H_2$ environment during the cooling stage aims to etch multilayer nucleation sites resulting from carbon supersaturation of the Pt foil. Next, a PMMA layer was spin coated on the graphene to protect and maintain structural integrity during transfer. The PMMA/Gr/Pt stack was then put in a deionized water bath at 80 °C for 18 h to promote water intercalation in between the graphene and Pt foil. Subsequently, a frame was glued onto the PMMA/Gr/Pt stack to assist in handling the graphene after delamination and facilitating alignment with the target substrate. Afterwards, a wet electrochemical method was used to transfer graphene to the monolayer $WS_2$ or 90 nm $SiO_2$ substrate, which is described in detail elsewhere[65]. Essentially, graphene is delaminated from the Pt growth foil by the intercalation of cations which do not reduce within the electrochemical window of TEAH solvent. The ion intercalation was identified as the critical component for delamination rather than the hydrogen bubble formation resulting from the redox reaction of water at the Pt interface. Then, the graphene layer was rinsed and put to float in a deionized water bath and laminated onto the target substrate by lowering the water level, with help of a specially designed substrate holder and the frame glued on the PMMA/Gr stack. After lamination, the sample holder was placed on a hotplate at 80 °C under an angle of 45° to gently remove the water trapped in between the graphene and target substrate. After several hours, the stack was cut out of the frame and placed into a vacuum chamber on a hotplate at 50 °C overnight to further remove any residual water. In addition, XPS measurements show no Pt residues after graphene transfer that would otherwise degrade the interface quality (see Supplementary information, Supplementary Fig. 9).

### Solvent treatment

The solvent treatment consisted of an overnight (±12 h) acetone dip, followed by a short (5 min) isopropanol dip to remove acetone residues. Both solvent treatments were carried out at room temperature.

### $H_2$ Downstream Plasma Source treatment

A Lam Research downstream plasma etch system (2300 Microwave stripper) was used to carry out the $H_2$ dry cleaning treatments. Graphene coupons were placed in 300 mm silicon pocket wafers for processing. The etching process consisted of a 60 s heat-up step at 300 °C, followed by a low-power $H_2$ DPS exposure for which a highly diluted plasma chemistry was used i.e., $He/H_2$ 5000/50 sccm ratio at 300 °C, 1 Torr and 500 W plasma power[37]. A pre-conditioning was performed prior to the graphene dry cleaning, to clean out the chamber and avoid carry-over-effects from preceding plasma processes. This pre-conditioning used $He/H_2$ chemistry in a 3000/900 sccm ratio at 300 °C,1 Torr and 1000 W plasma power. The cleanliness of the graphene surface was then verified by tip cleaning AFM, explained further on.

### Graphene $UV/O_3$ oxidation

A UVO-Cleaner Model 144AX (Jelight) was used to carry out the $UV/O_3$ treatment with an oxygen gas flow of 300 L $h^{-1}$, without additional sample heating, the reaction chamber at room temperature and atmospheric pressure, and a mercury lamp as UV source (Power settings: 100–120 V, 60 Hz), located above the sample surface.

### $HfO_2$ atomic layer deposition

$HfO_2$ ALD was carried out in a 300 mm ASM Eagle XP4 tool (cross flow ALD reactor). The ALD precursors used were hafnium (IV) chloride and water (pulsed first) at a temperature of 300 °C.

### Raman and photoluminescence spectroscopy

A Horiba Jobin-Yvon HR800 Raman tool was used for the Raman measurement on graphene and $WS_2$ with a 532 nm laser at 3 mW laser power (or 50% ND filter), 1000 μm confocal hole, 1800 grooves $mm^{-1}$ grating, 100 × 0.9 NA Olympus objective, and a double exposure of 2 (accumulations) x 30 s (integration time) with spike filter to eliminate cosmic spikes.

The Raman mappings consisted of a 20 × 20 $\mu$ m scan for which a 1 $\mu$ m step-size was used, shown in Fig. 2.

Note that direct peak comparison between the two sets of Raman spectra of the Gr/$WS_2$ and Gr/$SiO_2$ stacks (Fig. 5) is not possible since a significantly lower laser intensity was used for the Gr/$WS_2$ stack. This is because the high laser intensity, typically used for graphene, can induce $WS_2$ oxidation in the presence of intercalated water originating from ambient or the wet transfer process used in this work[66]. Nevertheless, the claims made regarding the graphene layer remain valid since no similar quenching is observed for graphene on $WS_2$ compared to graphene on $SiO_2$ after 30 min of UV/$O_3$ exposure, as shown in Fig. 5.

A Horiba Jobin–Yvon HR800 Raman tool was used for the PL measurements on $WS_2$ with a 532 nm laser at 0.05 mW laser power (or 1% ND filter), 1000 µm confocal hole, 600 grooves $mm^{-1}$ grating, 100 × 0.9 NA Olympus objective, and a double exposure of 1 (accumulations) x 15 s (integration time) with spike filter to eliminate cosmic spikes.

### Water contact angle

An OCA contact angle system (Dataphysics) was used with a standard CCD camera (768×576 25 fps intercalated), Hamilton 500 µL syringe and needle thickness of 0.52 mm. A water droplet was dispensed onto the sample surface by manually lowering and lifting the syringe set-up. Sufficient time (~30 s) was taken for the droplet to reach equilibrium wetting, after which a snapshot was made and used to calculate the contact angle of the water droplet and sample surface (Static WCA method). The CA measurements were performed within 5 min of UV/$O_3$ exposure to minimize the effect of ambient contamination.

### X-ray photoelectron spectroscopy

The measurements were carried out in Angle Integrated mode using a QUANTES instrument from Physical electronics. The measurements were performed using a monochromatized photon beam of 1486.6 eV, a 100 microns spot size with charge neutralization.

CasaXPS software was used to analyse and deconvolute the C*1s* and W*4f* spectra. In case of the W*4f* core level, the spectra were deconvoluted by fitting doublets corresponding to W(0) i.e., $WS_2$ at ±32 & 34 eV, W( + IV) i.e., $WO_2$ at ±34 & 36 eV and W( + VI) i.e., $WO_3$ at ±35.3 & 37.8[46], while respecting an area ratio of ¾ resulting from spin-orbit coupling[67]. An extra peak was added at high binding energy corresponding to the W$5p_{3/2}$ subshell[46]. A Lorentzian asymmetric line shape was used to extract the different peak contributions and normalized to account for any acquisition-related intensity variations. The deconvoluted spectra together with the peak numerical values are provided in the Supplementary g information (Supplementary Figs. 11, 12, 14).

### Rutherford backscattering spectroscopy

A 6SDH tandem accelerator (National Electrostatics Corporation) was used where the accelerated ions were magnetically examined to eliminate contaminants and determine the ion energy. Afterwards, the ion beam was collimated to 1 mm in size and introduced to the scattering chamber, where the sample was mounted on a manipulator. The experimental settings included a particle energy of 1.523 MeV, $He^+$ beam, scattering angle of 170°, sample tilt angle of 11°, a beam current of 22 nA and detector calibration with 68 KeV offset, 1.4925 KeV gain and a FWHM 0.1626E-01 MeV.

The error bars correspond to the absolute error, calculated via Eq. (1):

$$\sqrt{\left(\frac{Sum}{4}\right)^2 + (Sum * 0.02)^2} \quad (1)$$

Where Sum corresponds to the fitting value of the element in question i.e., the amount of the element in atoms $cm^{-2}$.

Since the RBS signals of Hf and W overlap, a reference $WS_2$ sample was measured to estimate the W signal contribution and was later subtracted in case of all samples that contained both Hf and W in their stack. This subtraction was also included in the error calculation.

### (Tip cleaning) Atomic force microscopy

Tip cleaning AFM was carried out using a Nanoscope V AFM tool (Bruker) in lateral force microscopy (LFM) mode under an angle of 90°. A HQ-NSC19/AIBs cantilever was used with a spring constant of ~0.5 N $m^{-1}$. Due to the low spring constant, scans were carried out with very small loading forces (<1 nN) that ensured the underlying graphene surface did not get damaged during the mechanical scratching process. Subsequent scans were performed in peak force QNM mode to determine the topography and contaminant thickness. Since this an oscillating type of mode, no lateral forces were exerted during the scans that could displace the residues over the graphene surface.

### Scanning electron microscopy

Top-down scanning electron microscopic images were recorded with a FEIS Verios™ apparatus using a 3 kV beam energy, 0.10 nA beam current, 5.0 µs dwell time, a through-the-lens detection system of secondary electrons with a horizontal field of view and a working distance of 2.6 mm.

### Transmission electron microscopy

Cross transmission electron microscopic images were recorded via the Titan[3] G2 60-300 (FEI) with a FEG electron source, operated at 200 kV. A spin-on-carbon (SOC) cap layer was deposited to protect the surface during the focused ion beam sample preparation.

### Graphene Field Effect Transistor fabrication and measurement

For GFET fabrication, a graphene layer was grown, transferred on 90 nm $SiO_2$/Si, and cleaned as described earlier. Next, graphene patterning was done via photolithography i.e., a positive resist (IX845) was spin coated and baked for 1 min at 120 °C before optical exposure. After, the resist/graphene stack was developed in OPD 5262 and etched using an oxygen plasma. After graphene patterning, the bulk resist was removed by the solvent treatment described earlier. Source and drain were deposited by lift-off using the same photolithography process and resist mentioned earlier. The metal contacts consist of 2 nm Ti / 50 nm Pd. After lift-off, the devices were again solvent treated and additionally cleaned by the $H_2$ DPS plasma protocol described earlier.

For device measurements, a Keithley 4200 parameter analyser was used with a Cascade probe station in ambient without light exposure during measurement. The gate voltage was swept by changing the potential applied to the chuck/sample holder i.e., a back gated set-up.

## Data availability

The data that support the findings of this study are available on request from the corresponding author.

## Code availability

The code used for Raman mapping and GFET analysis are available on request from the corresponding author.

Received: 22 September 2023; Accepted: 19 March 2024;
Published online: 27 March 2024

## References

1. Ding, J., et al. Properties, preparation, and application of tungsten disulfide: a review. *J. Phys. D Appl. Phys.* **54** 2021).
2. Huyghebaert, C. et al. 2D materials: roadmap to CMOS integration. *2018 IEEE Int. Electron Devices Meet (IEDM)* **1**, 512–515 (2018).
3. Das, S., Robinson, J. A., Dubey, M., Terrones, H. & Terrones, M. Beyond Graphene: progress in novel two-dimensional materials and van der Waals Solids. *Annu. Rev. Mater. Res.* **45**, 1–27 (2015).

4. Gong, C. et al. Electronic and optoelectronic applications based on 2D novel anisotropic transition metal dichalcogenides. *Adv. Sci.* **4**, 1700231 (2017).
5. Gong, C., et al. Band alignment of two-dimensional transition metal dichalcogenides: application in tunnel field effect transistors. *Appl. Phys. Lett*. **103** (2013).
6. McDonnell, S. J. & Wallace, R. M. Atomically-thin layered films for device applications based upon 2D TMDC materials. *Thin Solid Films* **616**, 482–501 (2016).
7. Nam, T., Seo, S. & Kim, H. Atomic layer deposition of a uniform thin film on two-dimensional transition metal dichalcogenides. *J. Vac. Sci. Technol. A* **38** (2020).
8. Daukiya, L., Seibel, J. & De Feyter, S. Chemical modification of 2D materials using molecules and assemblies of molecules. *Adv. Phys. X* **4**, (2019).
9. Vervuurt, R. H. J., Karasulu, B., Verheijen, M. A., Kessels, W. M. M. & Bol, A. A. Uniform atomic layer deposition of Al2O3 on graphene by reversible hydrogen plasma functionalization. *Chem. Mater.* **29**, 2090–2100 (2017).
10. Azcatl, A. et al. HfO2 on UV-O3 exposed transition metal dichalcogenides: Interfacial reactions study. *2D Mater*. **2**, (2015).
11. Azcatl, A. et al. MoS2 functionalization for ultra-thin atomic layer deposited dielectrics. *Appl. Phys. Lett*. **104**, (2014).
12. Zhao, P. et al. Understanding the impact of annealing on interface and border traps in the Cr/HfO2/Al2O3/MoS2System. *ACS Appl. Electron. Mater.* **1**, 1372–1377 (2019).
13. Zhao, P. et al. Probing interface defects in top-gated MoS2 transistors with impedance spectroscopy. *ACS Appl. Mater. Interfaces* **9**, 24348–24356 (2017).
14. Nyns, L. et al. Study of the surface reactions in ALD Hafnium aluminates. *J. Electrochem. Soc.* **157**, G7–G12 (2010).
15. Schilirò, E., Lo Nigro, R., Roccaforte, F., & Giannazzo, F. Recent advances in seeded and seed-layer-free atomic layer deposition of high-K dielectrics on graphene for electronics. *C J. Carbon Res*. **5** (2019).
16. Meric, I. et al. Channel length scaling in graphene field-effect transistors studied with pulsed current-voltage measurements. *Nano Lett.* **11**, 1093–1097 (2011).
17. Alaboson, J. M. P. et al. Seeding atomic layer deposition of high-k dielectrics on epitaxial graphene with organic self-assembled monolayers. *ACS Nano* **5**, 5223–5232 (2011).
18. Fallahazad, B. et al. Scaling of Al2O3 dielectric for graphene field-effect transistors. *Appl. Phys. Lett.* **100**(9), 093112 (2012).
19. Wang, X., Tabakman, S. M. & Dai, H. Atomic layer deposition of metal oxides on pristine and functionalized graphene. *J. Am. Chem. Soc.* **130**, 8152–8153 (2008).
20. Mali, K. S., Greenwood, J., Adisoejoso, J., Phillipson, R. & De Feyter, S. Nanostructuring graphene for controlled and reproducible functionalization. *Nanoscale* **7**, 1566–1585 (2015).
21. Rodríguez González, M. C. et al. Self-limiting covalent modification of carbon surfaces: Diazonium chemistry with a twist. *Nanoscale* **12**, 18782–18789 (2020).
22. Nourbakhsh, A. et al. Graphene oxide monolayers as atomically thin seeding layers for atomic layer deposition of metal oxides. *Nanoscale* **7**, 10781–10789 (2015).
23. Sruthi, T. & Tarafder, K. Enhancement of quantum capacitance by chemical modification of graphene supercapacitor electrodes: a study by first principles. *Bull. Mater. Sci.* **42**, 1–6 (2019).
24. Qian, F. et al. Transistors and logic circuits enabled by 2D transition metal dichalcogenides: a state-of-the-art survey. *J. Mater. Chem. C* **10**, 17002–17026 (2022).
25. Yang, T. et al. Mechanical sensors based on two-dimensional materials: sensing mechanisms, structural designs and wearable applications. *iScience* **25**, 103728–103728 (2022).
26. Gao, J. et al. Aging of transition metal dichalcogenide monolayers. *ACS Nano* **10**, 2628–2635 (2016).
27. Kotsakidis, J. C. et al. Oxidation of monolayer WS2 in ambient is a photoinduced process. *Nano Lett.* **19**, 5205–5215 (2019).
28. Chang, Y. P. et al. Oxidation and degradation of WS2 monolayers grown by NaCl-assisted chemical vapor deposition: mechanism and prevention. *Nanoscale* **13**, 16629–16640 (2021).
29. Lin, L., Deng, B., Sun, J., Peng, H. & Liu, Z. Bridging the gap between reality and ideal in chemical vapor deposition growth of graphene. *Chem. Rev.* **118**, 9281–9343 (2018).
30. Liang, J. et al. Impact of post-lithography polymer residue on the electrical characteristics of MoS 2 and WSe 2 field effect transistors. *Adv. Mater. Interfaces* **6**, 1–10 (2019).
31. Cunge, G. et al. Dry efficient cleaning of poly-methyl-methacrylate residues from graphene with high-density H-2 and H-2-N-2 plasmas. *J. Appl. Phys.* **118**, 123302 (2015).
32. Nasir, T. et al. Design of softened polystyrene for crack- and contamination-free large-area graphene transfer. *Nanoscale* **10**, 21865–21870 (2018).
33. Yang, X. & Yan, M. Removing contaminants from transferred CVD graphene. *Nano Res.* **13**, 599–610 (2020).
34. Lin, Y.-C. et al. Graphene annealing: how clean can it be? *Nano Lett.* **12**, 414–419 (2012).
35. Mehedi, H. A. et al. High density H2 and He plasmas: can they be used to treat graphene? *J. Appl. Phys*. **124**, (2018).
36. Peltekis, N. et al. The effect of downstream plasma treatments on graphene surfaces. *Carbon N. Y.* **50**, 395–403 (2012).
37. Marinov, D. et al. Reactive plasma cleaning and restoration of transition metal dichalcogenide monolayers. *npj 2D Mater. Appl.* **5**, 1–10 (2021).
38. Umemoto, H., Kato, T., Takiguchi, M., Takagi, S. & Horibe, H. Decomposition processes of photoresist polymers by H atoms produced on hot wire surfaces. *Thin Solid Films* **635**, 27–31 (2017).
39. Despiau-Pujo, E., Davydova, A., Cunge, G. & Graves, D. B. Hydrogen plasmas processing of graphene surfaces. *Plasma Chem. Plasma Process.* **36**, 213–229 (2016).
40. Wu, J. B., Lin, M. L., Cong, X., Liu, H. N. & Tan, P. H. Raman spectroscopy of graphene-based materials and its applications in related devices. *Chem. Soc. Rev.* **47**, 1822–1873 (2018).
41. Luo, Z. et al. Thickness-dependent reversible hydrogenation of graphene layers. *ACS Nano* **3**, 1781–1788 (2009).
42. Mulyana, Y., Uenuma, M., Ishikawa, Y. & Uraoka, Y. Reversible oxidation of graphene through ultraviolet/ozone treatment and its nonthermal reduction through ultraviolet irradiation. *J. Phys. Chem. C* **118**, 27372–27381 (2014).
43. Cheng, Y. C., Kaloni, T. P., Zhu, Z. Y. & Schwingenschlögl, U. Oxidation of graphene in ozone under ultraviolet light. *Appl. Phys. Lett*. **101** (2012).
44. Al-Gaashani, R., Najjar, A., Zakaria, Y., Mansour, S. & Atieh, M. A. XPS and structural studies of high quality graphene oxide and reduced graphene oxide prepared by different chemical oxidation methods. *Ceram. Int.* **45**, 14439–14448 (2019).
45. Kwan, Y. C. G., Ng, G. M. & Huan, C. H. A. Identification of functional groups and determination of carboxyl formation temperature in graphene oxide using the XPS O 1s spectrum. *Thin Solid Films* **590**, 40–48 (2015).
46. Groven, B., Tomczak, Y., Heyns, M., Radu, I. & Delabie, A. Two-dimensional WS2 crystals at predetermined locations by anisotropic

growth during atomic layer deposition. *J. Appl. Phys.* **128**, 175302 (2020).
47. Yu, W., Sisi, L., Haiyan, Y. & Jie, L. Progress in the functional modification of graphene/graphene oxide: a review. *RSC Adv.* **10**, 15328–15345 (2020).
48. Gammelgaard, L. et al. Graphene transport properties upon exposure to PMMA processing and heat treatments. *2D Mater.* **1**, 35005–35011 (2014).
49. Sundararajan, A., Boland, M. J., Patrick Hunley, D. & Strachan, D. R. Doping and hysteretic switching of polymer-encapsulated graphene field effect devices. *Appl. Phys. Lett.* **103**, 253505 (2013).
50. Sun, J., Finklea, H. O. & Liu, Y. Characterization and electrolytic cleaning of poly(methyl methacrylate) residues on transferred chemical vapor deposited graphene. *Nanotechnology* **28**, 125703–125703 (2017).
51. Achra, S. et al. Enhancing interface doping in graphene-metal hybrid devices using H2 plasma clean. *Appl. Surf. Sci.* **538**, 148046 (2021).
52. de la Rosa, C. J. L. et al. Insight on the characterization of MoS 2 based devices and requirements for logic device integration. *ECS J. Solid State Sci. Technol.* **5**, 3072–3081 (2016).
53. Iwasaki, T., Muruganathan, M., Schmidt, M. E. & Mizuta, H. Partial hydrogenation induced interaction in a graphene-SiO2 interface: Irreversible modulation of device characteristics. *Nanoscale* **9**, 1662–1669 (2017).
54. Jia, Y. et al. Toward high carrier mobility and low contact resistance: laser cleaning of PMMA residues on graphene surfaces. *Nano Micro Lett.* **8**, 336–346 (2016).
55. Farmer, D. B. et al. Chemical doping and electron-hole conduction asymmetry in graphene devices. *Nano Lett.* **9**, 388–392 (2009).
56. Šljivančanin, Ž., Milošević, A. S., Popović, Z. S. & Vukajlović, F. R. Binding of atomic oxygen on graphene from small epoxy clusters to a fully oxidized surface. *Carbon N. Y.* **54**, 482–488 (2013).
57. Cheng, Y. C., Kaloni, T. P., Zhu, Z. Y. & Schwingenschlögl, U. Oxidation of graphene in ozone under ultraviolet light. *Appl. Phys. Lett.* **101**, 073110 (2012).
58. Shunaev, V. V. & Glukhova, O. E. Topology influence on the process of graphene functionalization by epoxy and hydroxyl groups. *J. Phys. Chem. C* **120**, 4145–4149 (2016).
59. Liu, Y., Zhang, J., Meng, S., Yam, C. & Frauenheim, T. Electric field tunable ultrafast interlayer charge transfer in Graphene/ WS2Heterostructure. *Nano Lett.* **21**, 4403–4409 (2021).
60. Henck, H. et al. Electronic band structure of Two-Dimensional WS2 /Graphene van der Waals Heterostructures. *Phys. Rev. B* **97** (2018).
61. Zhou, M., Wang, W., Lu, J. & Ni, Z. How defects influence the photoluminescence of TMDCs. *Nano Res.* **14**, 29–39 (2021).
62. Lee, J. U. & Cheong, H. Resonance Raman effects in transition metal dichalcogenides. *J. Raman Spectrosc.* **49**, 66–75 (2018).
63. Kang, M., Yang, H. I. & Choi, W. Oxidation of WS2 and WSe2 monolayers by ultraviolet-ozone treatment. *J. Phys. D Appl. Phys*. **52** (2019).
64. Verguts, K. et al. Growth of millimeter-sized graphene single crystals on Al2O3 (0001)/Pt(111) template wafers using chemical vapor deposition. *ECS J. Solid State Sci. Technol.* **7**, 195–200 (2018).
65. Verguts, K. et al. Graphene delamination using 'electrochemical methods': An ion intercalation effect. *Nanoscale* **10**, 5515–5521 (2018).
66. Atkin, P. et al. Laser exposure induced alteration of WS2 monolayers in the presence of ambient moisture. *2D Mater.* **5**, 015013 (2018).
67. Major, G. H. et al. Practical guide for curve fitting in x-ray photoelectron spectroscopy. *J. Vac. Sci. Technol. A* **38** (2020).

## Acknowledgements

The project leading to this publication has received funding from the European Union's Horizon 2020 research and innovation program Graphene Flagship 2D Experimental Pilot Line (2D-EPL), Grant no. 952792. The authors thank Dr. Benjamin Groven for supplying the monolayer $WS_2$ material used in this study.

## Author contributions

The manuscript was written by P.-J.W. with contributions from J.-F.d.M. and S.D.G. The manuscript was revised and approved by all co-authors. P.-J.W. carried out all experimental work needed for the data generation provided in the manuscript and performing the optical (Raman & PL) and water contact angle measurements. J.-F.d.M. was involved in all discussions regarding data analysis and interpretation, and coordination of the SEM characterization. S.S. carried out all AFM tip cleaning characterizations, graphene Raman mappings, and engaged in discussions regarding optical characterizations. C.J.L.d.l.R. supported the GFET fabrication, measurements, and device analysis. S.B. and A.M.C. accommodated the graphene material supply and were involved in discussions and data analysis surrounding graphene cleaning, and $Gr/WS_2$ heterostructure fabrication. S.D.G. was involved in all discussions involving data analysis and interpretation.

## Competing interests

The authors declare no competing interests.

## Additional information

**Supplementary information** The online version contains supplementary material available at https://doi.org/10.1038/s41699-024-00464-x.

**Correspondence** and requests for materials should be addressed to P.-J. Wyndaele.